mathematics

MDPI

Article

Slow Translation of a Soft Sphere in an Unbounded Micropolar Fluid with Interfacial Stress Jump

Shreen El-Sapa

Department of Mathematical Sciences, College of Science, Princess Nourah bint Abdulrahman University, P.O. Box 84428, Riyadh 11671, Saudi Arabia; seelsapa@pnu.edu.sa

Abstract

This study presents a theoretical analysis of the slow translation of a soft sphere through an unbounded micropolar fluid under steady, low Reynolds number conditions, accounting for the influence of interfacial stress jump. The soft sphere is modeled as a rigid solid core surrounded by a permeable porous gel layer, allowing fluid penetration and momentum exchange across the interface. This core–shell configuration captures the essential structural characteristics of coated or gel-like particles encountered in biological and engineering systems. Closed-form expressions for the velocity components, microrotation, stresses, and couple stresses are derived both within the porous micropolar gel layer surrounding the particle and in the exterior micropolar fluid. The flow inside the permeable coating is described using the general Brinkman solution in spherical coordinates, while the governing micropolar fluid equations are applied in the outer region. Appropriate boundary conditions are imposed at the solid core surface and at the permeable soft-sphere interface to ensure continuity of velocity and microrotation, together with the prescribed stress jump. The normalized drag force acting on the particle is obtained as a function of the particle-to-core radius ratio, permeability, stress-jump parameter, and micropolarity parameter. The results indicate that the hydrodynamic drag decreases as the porous layer becomes thicker and remains finite, approaching unity even when the soft sphere behaves as a solid particle or as a porous sphere translating through an infinite micropolar medium, with other parameters held fixed. Overall, the analysis elucidates the coupled roles of micropolar effects, interfacial stress jump, and porous-layer structure in governing the hydrodynamic resistance experienced by soft particles.

Keywords: soft sphere; micropolar; stress jump; hydrodynamic drag; slow motion

MSC: 74F10

Check for updates

Academic Editor: John Venetis

Received: 22 January 2026

Revised: 13 February 2026

Accepted: 16 February 2026

Published: 21 February 2026

Correction Statement: This article has been republished with a minor change. The change does not affect the scientific content of the article and further details are available within the backmatter of the website version of this article.

1. Introduction

Soft-sphere models are essential for describing the behavior of deformable particles whose interactions, governed by elasticity, surface tension, and contact forces, deviate from the rigid-body assumptions of classical mechanics [1]. By explicitly capturing elastic deformation, energy dissipation, and particle overlaps, these models provide greater physical realism for simulating complex systems such as granular flows, colloidal suspensions, and polymeric materials [2]. This capability is particularly valuable in engineering applications, where soft-sphere formulations in discrete element methods (DEM) are widely used to analyze processes like powder handling, pharmaceutical tablet coating, and particulate transport, as their accurate depiction of particle softness directly informs flow behavior and product quality [3]. Furthermore, the framework extends to biomedical applications, where modeling soft polymeric or hydrogel-based spheres is crucial for designing drug-delivery systems with controlled release and targeted transport [4]. Consequently, the versatility of soft-sphere models establishes a powerful, unified framework for understanding and designing advanced soft-matter systems across physics, engineering, and biomedical science.

The transport of soft spheres through porous media introduces a complex interplay between particle deformability, pore-scale geometry, and fluid-solid interactions [5]. This deformability allows particles to squeeze through constrictions inaccessible to rigid bodies, dynamically altering permeability, clogging behavior, and transport efficiency—a critical factor in processes like filtration and enhanced oil recovery. Consequently, the coupling of elastic deformation with pore-scale flow creates nonlinear mobility patterns that directly influence the medium's effective porosity and flow resistance [6]. In biomedical contexts, these mechanics are fundamental for modeling the migration of cells, vesicles, or therapeutic carriers through porous tissues and vascular networks, providing key insights for targeted drug delivery and understanding disease progression [7]. Thus, integrating soft-particle mechanics with porous-media theory is essential for accurately predicting and optimizing transport in both natural and engineered systems.

Micropolar fluid theory extends classical continuum mechanics by incorporating micro-rotational degrees of freedom, couple stresses, and intrinsic angular momentum, making it a critical framework for modeling complex fluids with internal microstructure [8]. This theory can accurately describe fluids such as blood, polymeric suspensions, liquid crystals, and lubricants containing microelements, capturing behaviors like asymmetric stress and particle rotation that Newtonian models cannot replicate [9]. Its enhanced descriptive power has led to significant applications in biomedical engineering, where it improves predictions of hemodynamics, and in tribology, where micropolar lubricants enhance load-bearing capacity and stability in bearings and microelectromechanical systems (MEMS) [10,11]. By offering deeper insight into flow stability and transport phenomena at small scales, micropolar models have become indispensable for modern research in advanced manufacturing, microfluidics, and materials science. Consequently, micropolar fluid mechanics continues to expand through diverse analytical and semi-analytical investigations, as demonstrated in studies ranging from the interaction of non-concentric spheres in micropolar media [12] to cell model analyses of porous micropolar droplets with stress jump conditions [13]. Complementary advances in confined particle hydrodynamics include the steady low Reynolds number rotation of a chain of coaxial soft spheres about the axis in a viscous fluid [14] and the translation of composite spheres in eccentric cavities [15], both employing collocation-based hybrid solutions to Brinkman–Stokes systems. Related progress in interfacial microhydrodynamics is reflected in the recent analysis of soft colloidal particles moving normal to planar fluid–fluid interfaces [16]. Beyond micropolar and porous media flows, a set of governing equations is developed to describe the unsteady flow of an incompressible polar fluid through isotropic porous sediments, employing the intrinsic volume-averaging method. The modeling of Darcy resistance accounts for the underlying porous microstructure, thereby demonstrating the contribution of rotational viscosity to the viscous shear term. The proposed formulation holds potential relevance for lubrication analyses involving porous configurations, the study of polymeric and oil flows within porous matrices, and investigations of blood transport through engineered micro-channels [17].

In this work, we develop a theoretical model for the slow translation of a soft spherical particle through an unbounded micropolar fluid under steady, low Reynolds number conditions, incorporating the effects of interfacial stress jump. The Brinkman solution describes the flow inside the porous coating, while micropolar fluid equations govern the exterior region, with boundary conditions ensuring continuity of velocity, microrotation, and stresses across the interfaces. A normalized drag expression is derived in terms of the core to particle radius ratio, permeability, stress jump parameter, and micropolarity. The results show that the hydrodynamic resistance decreases as the porous layer thickens and approaches finite limiting values consistent with both solid sphere and fully porous sphere behavior. This framework clarifies how micropolar effects and interfacial stress jumps jointly influence the motion of soft particles.

2. Field Equations Inside the Porous Region

The governing equations for the steady flow in a porous medium saturated by an incompressible micropolar fluid under the assumptions of low Reynolds numbers, in the absence of body force and body couples, are given by [10,16,17]

$$0 = \nabla \cdot \vec{q}^{(1)}, \tag{1}$$

$$0 = \nabla p^{(1)} + \frac{\mu+\kappa}{\varphi}\nabla \wedge \nabla \wedge \vec{q}^{(1)} - \frac{\kappa}{\varphi}\nabla \wedge \vec{v}^{(1)} + \frac{\mu+\kappa}{K}\vec{q}^{(1)}, \tag{2}$$

$$0 = (\alpha' + \beta + \gamma)\,\nabla(\nabla \cdot \vec{v}^{(1)}) - \gamma\nabla \wedge \nabla \wedge \vec{v}^{(1)} + \kappa\nabla \wedge \vec{q}^{(1)} - 2\kappa\vec{v}^{(1)}. \tag{3}$$

where $\vec{q}^{(1)}$ is the volume-averaged velocity vector, $\vec{v}^{(1)}$ is the volume-averaged microrotation vector, $p^{(1)}$ is the pore average pressure, μ is the dynamic viscosity coefficient, κ is the vortex viscosity, α and β are the bulk spin viscosity, γ is the shear spin viscosity, and K, φ are, respectively, the permeability and porosity of the porous medium. The quantity $\langle \nabla \cdot \vec{v} \rangle$ is the volume average of the divergence of the microrotation vector, defined by

$$\left\langle \nabla \cdot \vec{v}^{(1)} \right\rangle = \frac{1}{V}\int_V \nabla \cdot \vec{v}^{(1)}\, dV. \tag{4}$$

The governing Equations (1)–(4) were rigorously derived by Hamdan and Kamel [17] and subsequently analyzed by Khanukaeva and Filippov [18]. In the limiting case where $K \to 0$, the microrotation vector $\vec{v} = 0$, then Equation (2) simplifies to the classical Darcy-Brinkmann equation. Furthermore, in the absence of vortex viscosity coupling $\kappa = 0$, the velocity and microrotation fields decouple, rendering microrotation dynamically inert with respect to the macroscopic flow. The effective viscosity μ_e is generally distinct from the Newtonian dynamic viscosity μ, with equality only under the condition $\kappa = 0$. For high permeability $K \to \infty$, the above governing equations reduce to the Eringen equations for clear micropolar fluid flow [7].

The stress tensor, $\hat{\Pi}$ of the micropolar flow through the porous medium is a nonsymmetric tensor and is given by the following constitutive relation:

$$\vec{\Pi}^{(1)} = -p^{(1)}\vec{I} + \frac{\mu + \frac{1}{2}\kappa}{\varphi}\left(\nabla\vec{q}^{(1)} + \left(\nabla\vec{q}^{(1)}\right)^T\right) + \frac{\kappa}{\varphi}\vec{\epsilon} \cdot \left(\vec{\omega}^{(1)} - \vec{v}^{(1)}\right), \tag{5}$$

where $(\cdot)^T$ and the double arrow denotes, respectively to a transpose and a tensor, $\vec{I}$ is the unit dyadic, $\vec{\epsilon}$ is the unit triadic, and $\vec{\omega}^{(1)} = \frac{1}{2}\nabla \wedge \vec{q}^{(1)}$ is the vorticity vector. The symmetric part of the stress tensor $\vec{\Pi}$ in (4) is

$$\vec{\Pi}^{[S]} = -p^{(1)}\vec{I} + \frac{\mu + \frac{1}{2}\kappa}{\varphi}\left(\nabla\vec{q}^{(1)} + \left(\nabla\vec{q}^{(1)}\right)^T\right). \tag{6}$$

Consequently, the couple stress tensor $\vec{m}$ is represented by the following constitutive relation:

$$\vec{m}^{(1)} = \alpha' I \cdot \nabla\vec{v}^{(1)} + \beta\nabla\vec{v}^{(1)} + \gamma\left(\nabla\vec{v}^{(1)}\right)^T. \tag{7}$$

https://doi.org/10.3390/math14040732

3. Field Equations Inside the Unbounded Micropolar Region

The equations governing the flow of steady incompressible micropolar fluid in the absence of body force and body couples are given by [7,19]:

$$0 = \nabla \cdot \vec{q}^{(2)}, \tag{8}$$

$$0 = \nabla p^{(2)} + (\mu + \kappa)\nabla \wedge \nabla \wedge \vec{q}^{(2)} - \kappa \nabla \wedge \vec{v}^{(2)}, \tag{9}$$

$$0 = -\gamma \nabla \wedge \nabla \wedge \vec{v}^{(2)} + \kappa \nabla \wedge \vec{q}^{(2)} - 2\kappa \vec{v}^{(2)}, \tag{10}$$

where $\vec{q}^{(2)}$, $\vec{v}^{(2)}$, j and $p^{(2)}$ are the velocity vector, microrotation vector, density, microinertia and the fluid pressure at any point. The material constants μ is the viscosity coefficient of the classical viscous fluid, and κ and γ are the new viscosity coefficients for micropolar fluids. The constitutive equations for the stress tensor and the couple stress tensor are, respectively,

$$\vec{\Pi}^{(2)} = -p^{(2)}\vec{I} + (\mu + \tfrac{1}{2}\kappa)\left(\nabla \vec{q}^{(2)} + \left(\nabla \vec{q}^{(2)}\right)^T\right) + \kappa \vec{\epsilon} \cdot \left(\vec{\omega}^{(2)} - \vec{v}^{(2)}\right), \tag{11}$$

$$\vec{m}^{(2)} = \alpha' \vec{I} \cdot \nabla \vec{v}^{(2)} + \beta \nabla \vec{v}^{(2)} + \gamma \left(\nabla \vec{v}^{(2)}\right)^T. \tag{12}$$

where the comma denotes the partial differentiation, $\vec{I}$ and $\vec{\epsilon}$ are the Kronecker delta and the alternating tensor, respectively.

4. Mathematical Formulation of Soft Sphere Motion in Micropolar Fluid

In this section, we consider the axisymmetric flow problem. As depicted in Figure 1, the investigation concerns the creeping micropolar fluid flow regime of a homogeneous, constant-property fluid surrounding a soft spherical particle of outer radius (b), which undergoes uniform translation motion with velocity (U) along an axis perpendicular to its diameter. The particle is characterized by two concentric radii: the inner radius (a) and the outer radius (b), with the condition $(a < b)$. The spatial description employs the spherical coordinate system (r, θ, ϕ), referenced to the particle's geometric center. Structurally, the soft sphere consists of a rigid impermeable core of radius (a), enveloped by a permeable porous shell of thickness $(b - a)$, fully saturated with a micropolar fluid. Within this porous layer, the fluid velocity remains finite, whereas the external micropolar medium asymptotically approaches a quiescent state at large distances from the particle.

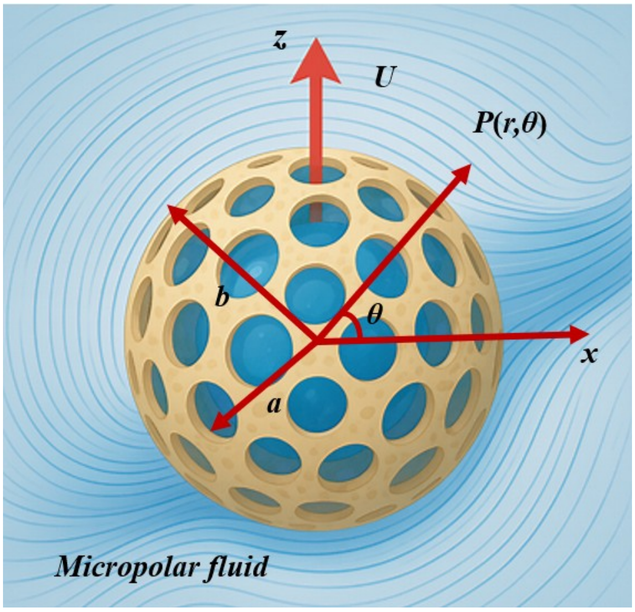

Figure 1. Schematic of the soft porous sphere in micropolar fluid.

4.1. Equation Satisfied by Stream Function and Its Solution Inside Porous Layer

This problem is axisymmetric, and all hydrodynamical variables are independent of ϕ. Therefore, the velocity and the microrotation vectors have the forms [10]:

$$\vec{q}^{(1)}(r,\theta) = q_r^{(1)}\vec{e}_r + q_\theta^{(1)}\vec{e}_\theta, \tag{13}$$

$$\vec{\nu}^{(1)}(r,\theta) = \nu_\phi^{(1)}\vec{e}_\phi. \tag{14}$$

Thus $\nabla \cdot \vec{\nu}^{(1)} = 0$ and thus $\left\langle \nabla \cdot \vec{\nu}^{(1)} \right\rangle = 0$. The velocity components can be written in terms of the stream function ψ as follows:

$$q_r^{(1)} = -\frac{1}{r^2 \sin\theta}\frac{\partial \psi^{(1)}}{\partial \theta}, \tag{15}$$

$$q_\theta^{(1)} = \frac{1}{r \sin\theta}\frac{\partial \psi^{(1)}}{\partial r}. \tag{16}$$

Using non-dimensional variables:

$$\left.\begin{aligned} \overline{r} = \frac{r}{a}, \overline{\psi} = \frac{\psi}{Ua^2}, \overline{\nu} = \frac{a\nu}{U}, \overline{\nabla} = a\nabla, \overline{q} = \frac{q}{U}, \alpha^2 = \frac{\varphi a^2}{K}, \\ m_{r\phi} = \frac{a^2 m_{r\phi}}{\beta U}, \tau_{r\phi} = \frac{\varphi a}{U(\mu+k)}\tau_{r\phi}, \tau_{rr} = \frac{\varphi a}{U(\mu+k)}\tau_{r\phi}, \overline{p} = \frac{\varphi a}{U(\mu+k)}p. \end{aligned}\right\} \tag{17}$$

From Equations (13)–(16) into (1)–(3) we get the following:

$$\frac{\partial p^{(1)}}{\partial r} = -\frac{1}{r^2 \sin\theta}\frac{\partial}{\partial \theta}\left(E^2 - \alpha^2\right)\psi^{(1)} + \frac{\kappa}{\mu+\kappa}\frac{1}{r\sin\theta}\frac{\partial}{\partial\theta}\left(\sin\theta\, \nu_\phi^{(1)}\right), \tag{18}$$

$$\frac{\partial p^{(1)}}{\partial \theta} = \frac{1}{\sin\theta}\frac{\partial}{\partial r}\left(E^2 - \alpha^2\right)\psi^{(1)} - \frac{\kappa}{\mu+\kappa}\frac{\partial}{\partial r}\left(r\, \nu_\phi^{(1)}\right), \tag{19}$$

$$E^2\left(r\sin\theta\, \nu_\phi^{(1)}\right) + \ell_0^2 E^2 \psi^{(1)} - 2\ell_0^2\left(r\sin\theta\, \nu_\phi^{(1)}\right) = 0. \tag{20}$$

Eliminating $p^{(1)}$, inserting the expressions (17) into the governing Equations (18)–(20), we obtain the differential equation satisfied by the stream function as follows:

$$E^2\left(E^2 - k_1^2\right)\left(E^2 - k_2^2\right)\psi^{(1)} = 0. \tag{21}$$

where $E^2 = \dfrac{\partial^2}{\partial r^2} + \dfrac{\sin\theta}{r^2}\dfrac{\partial}{\partial\theta}\left(\dfrac{1}{\sin\theta}\dfrac{\partial}{\partial\theta}\right)$ is the axisymmetric Stokesian operator,

$$\left.\begin{aligned} k_1^2 + k_2^2 = \alpha^2 + \ell^2, k_1^2 k_2^2 = 2\ell_0^2\alpha^2, \\ \ell_0^2 = \frac{a^2\kappa}{\gamma}, \alpha^2 = \frac{\varphi a^2}{K}, \ell^2 = \frac{2\mu+\kappa}{\mu+\kappa}\ell_0^2. \end{aligned}\right\} \tag{22}$$

All lengths are scaled with respect to the radius a. Explicit expressions for the roots k_1 and k_2 are as follows:

$$\left.\begin{aligned} k_1 = \sqrt{\frac{1}{2}\left(\ell^2 + \alpha^2\right) + \frac{1}{2}\sqrt{\left(\ell^2 + \alpha^2\right)^2 - 8\ell_0^2\alpha^2}}, \\ k_2 = \sqrt{\frac{1}{2}\left(\ell^2 + \alpha^2\right) - \frac{1}{2}\sqrt{\left(\ell^2 + \alpha^2\right)^2 - 8\ell_0^2\alpha^2}}. \end{aligned}\right\} \tag{23}$$

If we express $\psi^{(1)} = \psi_1^{(1)} + \psi_2^{(1)}$, then to satisfy (21) we have the following:

$$E^2\psi_1^{(1)} = 0, \tag{24}$$

$$\left(E^2 - k_1^2\right)\left(E^2 - k_2^2\right)\psi_2^{(1)} = 0. \tag{25}$$

The microrotation component is found to be, in terms of stream function, as

$$\left(r \sin\theta\, \nu_\phi^{(1)}\right) = \frac{\mu+\kappa}{\kappa}\left(E^2 - \alpha^2\right)\psi_2^{(1)}. \tag{26}$$

The general solution inside the porous region is as follows:

$$\psi^{(1)}(r,\theta) = \left[A_1 r^2 + \frac{B_1}{r} + \sum_{i=1}^{2} r^{\frac{1}{2}}\left(C_i I_{\frac{3}{2}}(k_i r) + D_i K_{\frac{3}{2}}(k_i r)\right)\right]\sin^2\theta. \tag{27}$$

The solutions for the velocity components, microrotation, and tangential stresses and couple stresses inside the porous region:

$$q_r^{(1)}(r,\theta) = -2\left[A_1 + \frac{B_1}{r^3} + r^{\frac{3}{2}}\sum_{i=1}^{2}\left(C_i I_{\frac{1}{2}}(k_i r) + D_i K_{\frac{1}{2}}(k_i r)\right)\right]\cos\theta, \tag{28}$$

$$q_\theta^{(1)}(r,\theta) = \left[2A_1 - \frac{B_1}{r^3} + r^{\frac{3}{2}}\sum_{i=1}^{2}\left(C_i\left(k_i I_{\frac{1}{2}}(k_i r) - I_{\frac{1}{2}}(k_i r)\right) - D_i\left(k_i r K_{\frac{1}{2}}(k_i r) + K_{\frac{1}{2}}(k_i r)\right)\right)\right]\sin\theta, \tag{29}$$

$$\nu_\phi^{(1)}(r,\theta) = \frac{\mu+\kappa}{\kappa}\sum_{i=1}^{2} r^{\frac{-3}{2}}\left(k_i^2 r^2 - \alpha^2\right)\left[C_i I_{\frac{1}{2}}(k_i r) + D_i K_{\frac{1}{2}}(k_i r)\right]\sin\theta, \quad m = \frac{\kappa}{\mu+\kappa}, \tag{30}$$

$$\begin{aligned}\tau_{r\theta}^{(1)}(r,\theta) = \Bigg[&-3r^{-4}B_1(m-2) + r^{\frac{-5}{2}}\sum_{i=1}^{2} C_i\left((\alpha^2 - 3m + 6)I_{\frac{1}{2}}(k_i r) + k_i r(m-2)I_{\frac{1}{2}}(k_i r)\right)\\ &+ D_i\left((\alpha^2 - 3m + 6)K_{\frac{1}{2}}(k_i r) - k_i r(m-2)K_{\frac{1}{2}}(k_i r)\right)\Bigg]\sin\theta.\end{aligned} \tag{31}$$

$$\begin{aligned}\tau_{rr}^{(1)}(r,\theta) = \Bigg[&-\alpha^2 A_1 r + \left(\alpha^2 r^2 - 6m + 12\right)B_1\\ &- 2(m-2)r^{\frac{-5}{2}}\sum_{i=1}^{2} C_i\left(3I_2(k_i r) + k_i r I_1(k_i r)\right) + D_i\left(3K_2(k_i r) + k_i r K_1(k_i r)\right)\Bigg]\cos\theta,\end{aligned} \tag{32}$$

$$\begin{aligned}m_{r\phi}^{(1)}(r,\theta) = \frac{1}{m}r^{\frac{\gamma}{2}}\sum_{i=1}^{2}\Bigg[&C_i\Bigg(\left((\alpha^2 - k_i^2 r^2) + \frac{2\gamma}{\beta}(2\alpha^2 + k_i^2 r^2)\right)I_{\frac{\gamma}{2}}(k_i r)\\ &- \frac{\gamma}{\beta}k_i r(\alpha^2 - k_i^2 r^2)I_{\frac{\gamma}{2}}(k_i r)\Bigg) + D_i\Bigg(\left((\alpha^2 - k_i^2 r^2) + \frac{2\gamma}{\beta}(2\alpha^2 + k_i^2 r^2)\right)K_{\frac{\gamma}{2}}(k_i r)\\ &+ \frac{\gamma}{\beta}k_i r(\alpha^2 - k_i^2 r^2)K_{\frac{\gamma}{2}}(k_i r)\Bigg)\Bigg]\sin\theta,\end{aligned} \tag{33}$$

where A, B, C_i, D_i are the hydrodynamical unknown constants to be evaluated, $I_{\frac{\gamma}{2}}(k_i r)$, $I_{\frac{\gamma}{2}}(k_i r)$ and $K_{\frac{\gamma}{2}}(k_i r)$, $K_{\frac{\gamma}{2}}(k_i r)$ are the modified Bessel functions of the second and first kinds, respectively.

4.2. Equation Satisfied by Stream Function and Its Solution Through Infinite Region

From the equation of continuity, it is satisfied automatically, and substitution in the field equations produces the following:

$$0 = -\frac{\partial p^{(2)}}{\partial r} - \frac{(\mu+\kappa)}{r^2\sin\theta}\frac{\partial}{\partial\theta}(L_{-1}\psi^{(2)}) + \frac{\kappa}{r\sin\theta}\frac{\partial}{\partial\theta}(\sin\theta\,\nu_\phi^{(2)}), \tag{34}$$

$$0 = -\frac{\partial p^{(2)}}{\partial\theta} + \frac{(\mu+\kappa)}{\sin\theta}\frac{\partial}{\partial r}(L_{-1}\psi^{(2)}) - \kappa\frac{\partial}{\partial r}(r\nu_\phi^{(2)}), \tag{35}$$

$$0 = \gamma L \nu_{\phi}^{(2)} + \kappa \frac{1}{r \sin\theta} L_{-1} \psi^{(2)} - 2\kappa \nu_{\phi}^{(2)}, \tag{36}$$

Eliminating pressure, we get the differential equation satisfied by the stream function as follows:

$$E^4 \left(E^2 - \ell^2 \right) \psi^{(2)} = 0, \tag{37}$$

The regular solutions for the stream function, the velocity components, microrotation, and tangential stresses and couple stresses inside the unbounded region:

$$\psi^{(2)}(r,\theta) = \left[A\, r^{-1} + B\, r + C\, r^{\frac{1}{2}} K_{\frac{3}{2}}(\ell r) \right] \sin^2\theta \tag{38}$$

$$q_r^{(2)}(r,\theta) = -2\left[A\, r^{-3} + B\, r^{-1} + C\, r^{\frac{-3}{2}} K_{\frac{1}{2}}(\ell r) \right] \cos\theta \tag{39}$$

$$q_\theta^{(2)}(r,\theta) = \left[-A\, r^{-3} + B\, r^{-1} - C\, r^{\frac{-3}{2}} \left(K_{\frac{1}{2}}(\ell r) + \ell r K_{\frac{1}{2}}(\ell r) \right) \right] \sin\theta \tag{40}$$

$$\nu_\phi^{(2)}(r,\theta) = \left[-B\, r^{-2} + \frac{\ell^2}{m} C\, r^{\frac{-3}{2}} K_{\frac{1}{2}}(\ell r) \right] \sin\theta \tag{41}$$

$$\tau_{r\theta}^{(2)}(r,\theta) = (2-m)\left[3B\, r^{-4} + D\, r^{\frac{-5}{2}} \left(3K_{\frac{1}{2}}(\ell r) + \ell r K_{\frac{1}{2}}(\ell r) \right) \right] \sin\theta \tag{42}$$

$$\tau_{rr}^{(2)}(r,\theta) = (2-m)\left[6A\, r^{-4} + 3B\, r^{-2} + 2C\, r^{\frac{-5}{2}} \left(3K_{\frac{1}{2}}(\ell r) + \ell r K_{\frac{1}{2}}(\ell r) \right) \right] \cos\theta \tag{43}$$

$$m_{r\phi}^{(2)}(r,\theta) = \left[(1 + 2\gamma\beta^{-1}) B\, r^{-3} - \frac{\ell^2}{m} C\, r^{\frac{-3}{2}} \left((1 + 2\gamma\beta^{-1}) K_{\frac{1}{2}}(\ell r) + \gamma\beta^{-1} \ell r K_{\frac{1}{2}}(\ell r) \right) \right] \sin\theta \tag{44}$$

where A, B, C are the hydrodynamical unknown constants to be evaluated.

4.3. Boundary Conditions at Fluid-Particle Interfaces

The solutions of Equations (28)–(33) and (38)–(44) are subject to the following conditions: **(i)** On the solid core $r = a$, the kinematic velocity, the dynamic stress, and the micropolar-specific (microrotation/couple stress):

$$q_r^{(1)} = 0, \tag{45}$$

$$q_\theta^{(1)} = 0, \tag{46}$$

$$\nu_\phi^{(1)} = 0. \tag{47}$$

(ii) On the soft sphere $r = b$, the interface conditions require continuity of velocity components, stress tensors, and couple stresses such that

$$q_r^{(1)} = U\cos\theta + q_r^{(2)}, \tag{48}$$

$$q_\theta^{(1)} = -U\sin\theta + q_\theta^{(2)}, \tag{49}$$

$$\nu_\phi^{(1)} = \nu_\phi^{(2)}, \tag{50}$$

$$t_{rr}^{(1)} = t_{rr}^{(2)}, \tag{51}$$

$$t_{r\theta}^{(1)} = t_{r\theta}^{(2)} + \frac{\alpha\mu\xi}{\mu + \kappa}, \tag{52}$$

$$m_{r\phi}^{(1)} = m_{r\phi}^{(2)}. \tag{53}$$

Here, $t_{rr}^{(1)}$, $t_{r\theta}^{(1)}$, $m_{r\phi}^{(1)}$ and $t_{rr}^{(2)}$, $t_{r\theta}^{(2)}$, $m_{r\phi}^{(2)}$ are the normal and tangential stresses in the porous and free flow regions ξ is the stress jump coefficient. In the range of negative values of stress jump coefficient, the shear stress of external free flow region becomes more than that of the internal (porous) flow region, which generates a significant drag force on the porous surface for any permeability. However, for positive values of ξ although the shear stress of the external region becomes low, but for a particular range of permeability, a significant drag force is generated on the surface. Hence, for both the basic flows, the stress jump boundary condition applied on the fluid–porous interface has a remarkable effect on the drag force. Note that if we put $\xi = 0$ (no jump in the shear stress at the interface) in the above boundary conditions, we get the corresponding conditions, which are due to continuity of velocity components and continuity of stress components.

4.4. Normalized Drag Force on the Soft Sphere

The drag force acting on a rigid body of revolution has the form [20]:

$$F_z = 4\pi(2\mu+\kappa)\lim_{r\to\infty}\left(\frac{r\psi^{(2)}(r,\theta)}{\rho^2}\right). \tag{54}$$

To determine the unknown constants A_1, B_1, C_i, D_i $(i = 1, 2)$ and A, B, C, we apply the boundary conditions (45)–(53) to expressions (28) to (33) and (38) to (45)–(53), we obtain the following system:

$$-2A_1 - 2B_1a^{-3} - 2a^{\frac{3}{2}}\sum_{i=1}^{2}\left(C_iI_{\frac{1}{2}}(k_ia) + D_iK_{\frac{1}{2}}(k_ia)\right) = U, \tag{55}$$

$$2A_1 - B_1a^{-3} + a^{\frac{3}{2}}\sum_{i=1}^{2}\left(C_i(k_iaI_{\frac{1}{2}}(k_ia) - I_{\frac{1}{2}}(k_ia)) - D_i(k_iaK_{\frac{1}{2}}(k_ia) + K_{\frac{1}{2}}(k_ia))\right) = -U, \tag{56}$$

$$\sum_{i=1}^{2}a^{\frac{3}{2}}(k_i^2a^2 - \alpha^2)\left[C_iI_{\frac{1}{2}}(k_ia) + D_iK_{\frac{1}{2}}(k_ia)\right] = 0, \tag{57}$$

$$A_1 + B_1b^{-3} + b^{\frac{3}{2}}\sum_{i=1}^{2}\left(C_iI_{\frac{1}{2}}(k_ib) + D_iK_{\frac{1}{2}}(k_ib)\right) = Ab^{-3} + Bb^{-1} + Cb^{\frac{3}{2}}K_{\frac{1}{2}}(\ell b) \tag{58}$$

$$\begin{aligned}&2A_1 - B_1b^{-3} + b^{\frac{3}{2}}\sum_{i=1}^{2}\left(C_i\left(k_ibI_{\frac{1}{2}}(k_ib) - I_{\frac{1}{2}}(k_ib)\right) - D_i\left(k_ibK_{\frac{1}{2}}(k_ib) + K_{\frac{1}{2}}(k_ib)\right)\right)\\&= -Ab^{-3} + Bb^{-1} - Cb^{\frac{3}{2}}\left(K_{\frac{1}{2}}(\ell b) + \ell bK_{\frac{1}{2}}(\ell b)\right)\end{aligned} \tag{59}$$

$$m^{-1}b^{\frac{3}{2}}\sum_{i=1}^{2}\left(k_i^2b^2 - \alpha^2\right)\left[C_iI_{\frac{1}{2}}(k_ib) + D_iK_{\frac{1}{2}}(k_ib)\right] = -Bb^{-2} + \ell^2m^{-1}Cb^{\frac{3}{2}}K_{\frac{1}{2}}(\ell b) \tag{60}$$

$$\begin{aligned}&-2z_1A_1 + \left[-3b^{-4}(m-2) + z_1b^{-3}\right]B_1\\&+ b^{-\frac{5}{2}}\sum_{i=1}^{2}\Bigg[C_i\left((\alpha^2 - 3m + 6 + z_1)I_{\frac{3}{2}}(k_ib) + k_ib(m - 2 - z_1)I_{\frac{1}{2}}(k_ib)\right)\\&\quad + D_i\left((\alpha^2 - 3m + 6 + z_1)K_{\frac{3}{2}}(k_ib) - k_ib(m - 2 - z_1)K_{\frac{1}{2}}(k_ib)\right)\Bigg]\\&= (2-m)\left[3Bb^{-4} + Cb^{-\frac{5}{2}}\left(3K_{\frac{1}{2}}(\ell b) + \ell bK_{\frac{1}{2}}(\ell b)\right)\right],\quad z_1 = \frac{\alpha\xi}{1+\kappa}\end{aligned} \tag{61}$$

$$\begin{aligned}&-2\alpha^2A_1b + b^{-4}(\alpha^2b^2 - 6m + 12)B_1\\&-2(m-2)b^{-\frac{5}{2}}\sum_{i=1}^{2}\left[C_i\left(3I_{\frac{3}{2}}(k_ib) - k_ibI_{\frac{1}{2}}(k_ib)\right) + D_i\left(3K_{\frac{1}{2}}(k_ib) + k_ibK_{\frac{1}{2}}(k_ib)\right)\right]\\&= (2-m)\left[6Ab^{-4} + 3Bb^{-2} + 2Cb^{-\frac{5}{2}}\left(3K_{\frac{1}{2}}(\ell b) + \ell bK_{\frac{1}{2}}(\ell b)\right)\right]\end{aligned} \tag{62}$$

$$\frac{1}{m}b^{\frac{\gamma}{2}}\sum_{i=1}^{2}\Bigg[C_i\Bigg(\Big((\alpha^2-k_i^2b^2)+\frac{2\gamma}{\beta}(2\alpha^2+k_i^2b^2)\Big)I_{\frac{\gamma}{2}}(k_ib)-\frac{\gamma}{\beta}k_ib(\alpha^2-k_i^2b^2)I_{\frac{\gamma}{2}}(k_ib)\Bigg)$$
$$+D_i\Bigg(\Big((\alpha^2-k_i^2b^2)+\frac{2\gamma}{\beta}(2\alpha^2+k_i^2b^2)\Big)K_{\frac{\gamma}{2}}(k_ib)+\frac{\gamma}{\beta}k_ib(\alpha^2-k_i^2b^2)K_{\frac{\gamma}{2}}(k_ib)\Bigg)\Bigg]$$
$$=(1+2\gamma\beta^{-1})Bb^{-3}-\ell^2m^{-1}Cb^{\frac{-3}{2}}G(\ell b), \tag{63}$$

By solving the nine linear systems by Maple program, where only the coefficient B contributes to the hydrodynamic force acting on the spherical particle $r=b$. Substitution into the relation (54) results in the simple relation:

$$F_z=4\pi(2\mu+\kappa)B. \tag{64}$$

It is appropriate to non-dimensionalise the drag force in (43) by $F_\infty=-6\pi\mu bU$.

5. Comparison and Validation

(i) A solid sphere moves through an infinite micropolar medium ($b/a=1$) [19]:

The general solution is as follows:

$$\psi^{(2)}(r,\theta)=\Big[A_0\,r^{-1}+B_0\,r+C_0\,r^{\frac{1}{2}}\,K_{\frac{3}{2}}(\ell r)\Big]\sin^2\theta \tag{65}$$

Hence, the boundary conditions are as follows:

$$q_r^{(2)}=U\cos\theta,\quad q_\theta^{(2)}=-U\sin\theta,\quad \nu_\phi^{(2)}=0, \tag{66}$$

Therefore, we get the following system:

$$2A_0\,a^{-3}+2B_0\,a^{-1}+2C_0\,a^{\frac{3}{2}}\,K_{\frac{3}{2}}(\ell a)=-U, \tag{67}$$

$$-A_0\,a^{-3}+B_0\,a^{-1}-C_0\,a^{\frac{3}{2}}\Big(K_{\frac{3}{2}}(\ell a)+\ell aK_{\frac{1}{2}}(\ell a)\Big)=-U, \tag{68}$$

$$-B_0\,a^{-2}+\frac{\ell^2}{m}\,C_0\,a^{\frac{-1}{2}}\,K_{\frac{3}{2}}(\ell a)=0. \tag{69}$$

Accordingly, solving Equations (66)–(68) yields:

$$C_0=\frac{-3Ua^{\frac{1}{2}}}{(4\ell^2m^{-1}-2\ell)K_{\frac{1}{2}}(\ell a)}, \tag{70}$$

$$B_0=\frac{(-5\ell^2m^{-1}+2\ell)}{(4\ell^2m^{-1}-2\ell)}Ua, \tag{71}$$

$$A_0=-\frac{(-6\ell^2m^{-1}+2\ell)K_{\frac{1}{2}}(\ell a)+6K_{\frac{3}{2}}(\ell a)}{2a^{-3}(4\ell^2m^{-1}-2\ell)K_{\frac{1}{2}}(\ell a)}U. \tag{72}$$

The drag force is as follows:

$$F_z=2\pi(2\mu+\kappa)\frac{(-5\ell^2m^{-1}+2\ell)}{(4\ell^2m^{-1}-2\ell)}Ua. \tag{73}$$

(ii) A porous sphere moves through an infinite micropolar medium ($b\to\infty$, $a=0$) [10]:

The general solution inside the porous sphere is as follows:

$$\psi^{(1)}(r,\theta)=\Big[Dr^2+r^{\frac{1}{2}}EI_{\frac{1}{2}}(k_1r)+r^{\frac{1}{2}}FI_{\frac{1}{2}}(k_2r)\Big]\sin^2\theta. \tag{74}$$

The unknown constants are A, B, C, D, E, F are determined by employing the boundary conditions:

$$q_r^{(1)} = U\cos\theta + q_r^{(2)}, \quad q_\theta^{(1)} = -U\sin\theta + q_\theta^{(2)}, \quad \nu_\phi^{(1)} = \nu_\phi^{(2)}, \tag{75}$$

$$t_{rr}^{(1)} = t_{rr}^{(2)}, \quad t_{r\theta}^{(1)} = t_{r\theta}^{(2)}, \quad m_{r\phi}^{(1)} = m_{r\phi}^{(2)}. \tag{76}$$

Accordingly, solving the above six linear systems, we get the drag force in terms of only one constant B_0, such as

$$F_z = 4\pi(2\mu + \kappa)B_0. \tag{77}$$

6. Numerical Results and Parametric Studies

The radial and transverse velocity fields, microrotation profiles, and the distributions of stresses and couple stresses inside the porous layer and in the surrounding micropolar fluid are presented for various key parameters with certain ranges, including the micropolarity ratio $\kappa/\mu = (0.001\text{–}10)$, permeability $\alpha = (0.01\text{–}10)$, the size ratio $\sigma = b/a = (1.1\text{–}2)$, and stress-jump coefficient $\xi = (0\text{–}1)$, with $\epsilon = \gamma/\beta = 0.3$ fixed values for all figures except the last one. Figures 2–19 provide analytical and numerical results for the velocity, microrotation, stress, and couple-stress distributions, while Figures 20–23 and Table 1 display the normalized drag force graphically and numerically, respectively. The results obtained exhibit excellent agreement with previously reported studies.

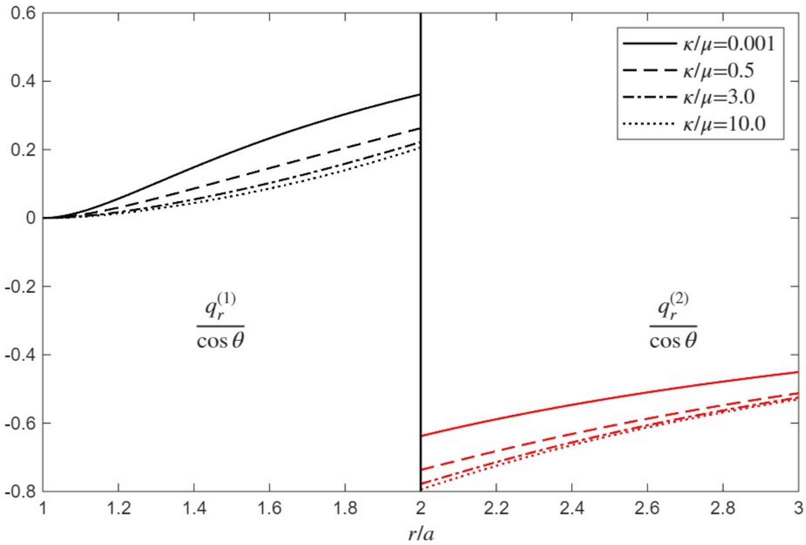

Figure 2. Normal velocity distribution for different micropolar parameters at $\xi = 0.01$, $\alpha = 2$.

Figures 2–7 express the field functions against the radial distance r/a for various micropolarity parameters at fixed size ratio, permeability, and stress jump. In Figure 2, inside the porous shell (1), the normal velocity $q_r^{(1)}$ decreases monotonically with increasing r/a, indicating a decaying radial flow away from the core. For lower micropolarity $\kappa/\mu = 0.1$, the decay is steep, while higher micropolarity $\kappa/\mu = 10$ flattens the profile, suggesting enhanced rotational coupling dampens radial motion. On the other hand, outside the soft sphere (2), the velocity profiles $q_r^{(2)}$ show similar decay trends, but with smoother gradients. Increased micropolarity reduces the magnitude of radial velocity, reflecting stronger resistance due to microstructure effects in the surrounding fluid.

In Figure 3, tangential velocity $q_\theta^{(1)}$ exhibits a peak near the interface and then decays. As κ/μ increases, the peak shifts outward and the magnitude reduces, indicating that micropolar effects suppress tangential motion. Hence, $q_\theta^{(2)}$ the profiles are smoother and more symmetrical. Higher micropolarity leads to flatter curves, showing reduced tangential flow due to enhanced microrotation coupling. In Figure 4, inside the porous layer, microrotation $\nu_\phi^{(1)}$ increases with r/a up to a peak and then decays. Larger κ/μ values amplify microrotation near the interface, consistent with stronger microstructural activity. Through the unbound medium, the microrotation $\nu_\phi^{(2)}$ is lower in magnitude and decays more gradually. Higher micropolarity enhances rotational effects but also spreads them over a wider radial range.

Table 1. Normalized drag force for different parameter values.

σ	κ/μ	$\xi = 0.0$				$\xi = 0.5$			
		$\alpha = 0.01$	$\alpha = 2.0$	$\alpha = 4.0$	$\alpha = 10.0$	$\alpha = 0.1$	$\alpha = 2.0$	$\alpha = 4.0$	$\alpha = 10.0$
1.1	0.001	0.86963	0.87617	0.89511	1.00400	0.86905	0.86469	0.87311	0.96194
	2	0.90178	0.90378	0.90944	0.93893	0.90170	0.90208	0.90622	0.93304
	4	0.90365	0.90530	0.91000	0.93426	0.90360	0.90437	0.90823	0.93102
	6	0.90401	0.90553	0.90983	0.93191	0.90398	0.90489	0.90861	0.92969
	8	0.90401	0.90545	0.90952	0.93043	0.90398	0.90496	0.90861	0.92875
	10	0.90387	0.90527	0.90921	0.92938	0.90385	0.90488	0.90847	0.92803
1.4	0.001	0.48972	0.63781	1.01490	2.32880	0.48606	0.57154	0.91412	2.24630
	2	0.61038	0.67527	0.78570	0.96225	0.60967	0.66371	0.77104	0.95272
	4	0.61307	0.67448	0.77571	0.93129	0.61265	0.66767	0.76719	0.92578
	6	0.61182	0.67286	0.77146	0.91889	0.61152	0.66800	0.76543	0.91502
	8	0.60999	0.67143	0.76916	0.91219	0.60975	0.66764	0.76449	0.90921
	10	0.60818	0.67026	0.76779	0.90802	0.60799	0.66715	0.76398	0.90560
2.0	0.001	0.18235	0.68111	1.76620	3.89630	0.17684	0.59312	1.65780	3.80640
	2	0.25224	0.50909	0.72901	0.94917	0.25073	0.49294	0.71537	0.94186
	4	0.25074	0.51078	0.71602	0.91733	0.24978	0.50097	0.70798	0.91309
	6	0.24880	0.51288	0.71196	0.90426	0.24808	0.50580	0.70625	0.90127
	8	0.24719	0.51457	0.71010	0.89684	0.24662	0.50902	0.70568	0.89454
	10	0.24590	0.51591	0.70911	0.89197	0.24542	0.51134	0.70549	0.89010

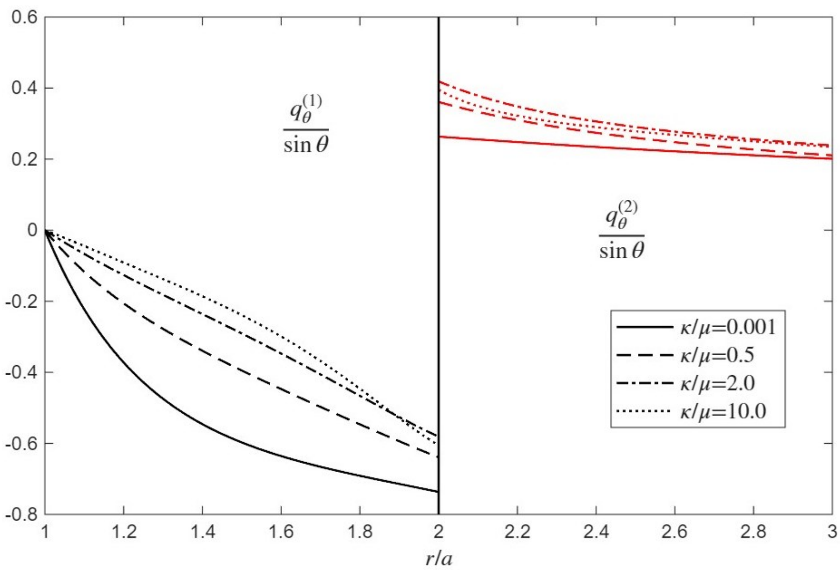

Figure 3. Tangential velocity distribution for different micropolar parameters at $\xi = 0.1$, $\alpha = 2$.

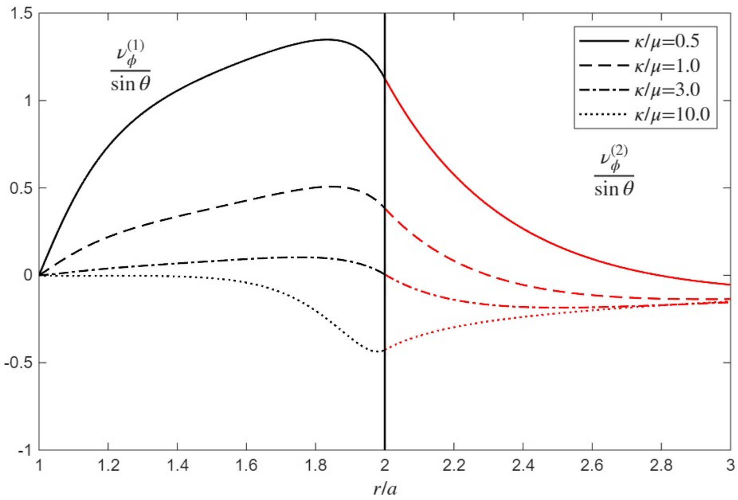

Figure 4. Microrotation distribution for different micropolar parameters at $\xi = 0.1,\ \alpha = 10$.

(1) Effects of micropolar parameter κ/μ:

In Figure 5, shear stress $\tau_{r\theta}^{(1)}$ shows a peak near the interface. As κ/μ increases, the peak shifts outward and the magnitude decreases, indicating that micropolarity reduces shear transmission. Also, the stress profiles $\tau_{r\theta}^{(2)}$ are smoother and lower in magnitude. Increased micropolarity leads to broader stress distributions, reflecting the damping effect of microrotation. Figure 6, the radial stress $\tau_{rr}^{(1)}$ decreases with r/a, with sharper gradients for low κ/μ. Higher micropolarity flattens the profile, indicating reduced stress concentration. Therefore, the stress $\tau_{rr}^{(2)}$ is more uniform and less sensitive to κ/μ, but still shows a decreasing trend. Micropolarity smooths the stress field, reducing peak values. In Figure 7, the couple stress $m_{r\phi}^{(1)}$ increases with r/a up to a peak and then decays. Higher κ/μ enhances the magnitude and shifts the peak outward, consistent with stronger rotational resistance. Furthermore, the couple stress $m_{r\phi}^{(2)}$ is lower and more spread out. Increased micropolarity leads to broader distributions, indicating that microrotation effects extend further into the fluid domain. The detailed analysis of velocity, microrotation, stress, and couple-stress fields for a soft porous sphere moving through a micropolar fluid has direct relevance to several applied systems where microstructural effects and interfacial resistance play a central role. In biomedical transport, the results help predict how coated drug-delivery capsules, microgels, or cells migrate through complex biological fluids that exhibit micropolar behavior, influencing drag, rotation, and deformation during motion. In microfluidic and lab-on-a-chip devices, understanding how micropolarity and porous layer properties modify flow resistance supports the design of more efficient platforms for particle manipulation, separation, and sensing. The findings also apply to porous media flows in enhanced oil recovery, where soft or coated particles move through microstructured fluids within permeable rock formations, thereby affecting mobility and pressure gradients. Additionally, industries dealing with emulsions, suspensions, and filtration—such as cosmetics, food processing, and membrane engineering—benefit from these insights, as the interplay between micropolarity, permeability, and interfacial stress jump governs particle stability, dispersion, and flow resistance in structured fluids.

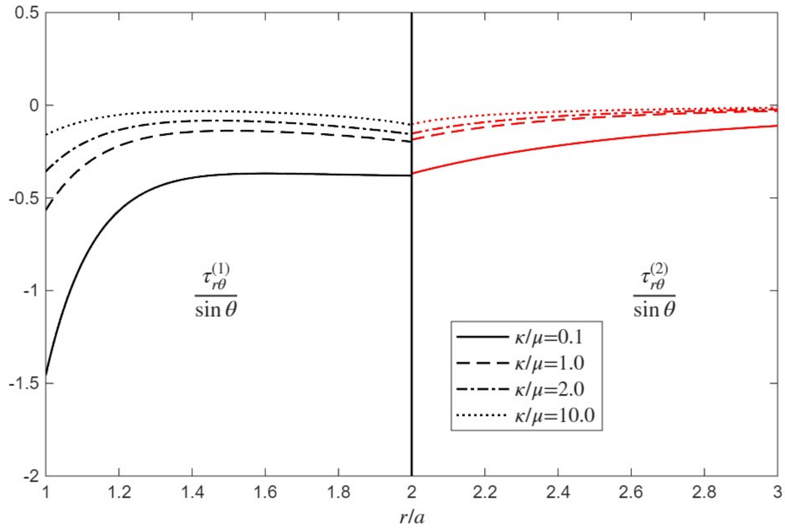

Figure 5. Tangential stress distribution for different micropolar parameters at $\xi = 0.01,\ \alpha = 3$.

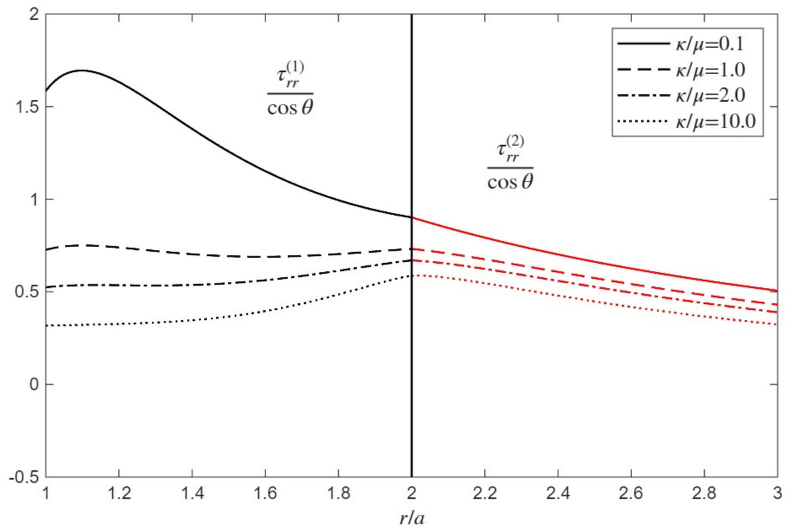

Figure 6. Normal stress distribution for different micropolar parameters at $\xi = 0.1,\ \alpha = 10$.

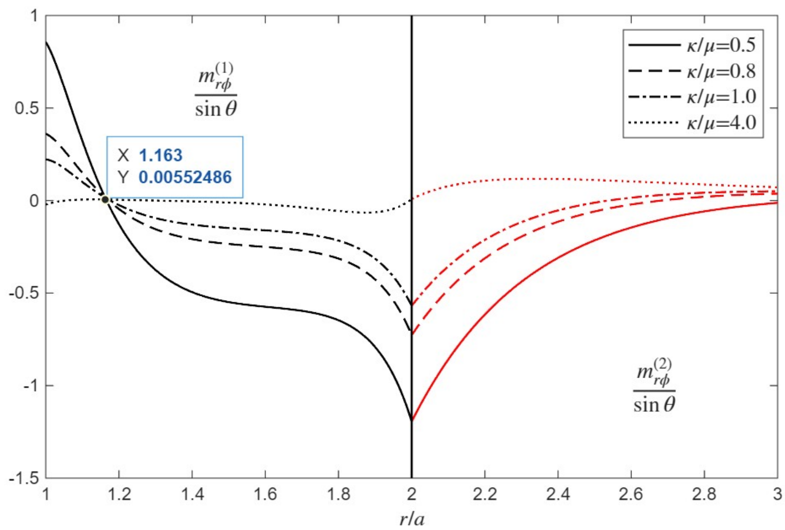

Figure 7. Tangential couple stress distribution for different micropolar parameters at $\xi = 0.01,\ \alpha = 3$.

(2) Effects of the permeability parameter α:

In Figure 8, the permeability α increases from 0.01 to 10.0, and the magnitude of the inward radial velocity decreases. This indicates that higher permeability allows more fluid to pass through with less resistance, reducing the pressure gradient across the shell. Outside the sphere (region 2), the radial velocity profiles become flatter with increasing α, showing smoother transitions at the interface. The fluid adjusts more gradually to the presence of the porous shell, reflecting reduced drag and enhanced flow continuity. Therefore, Figure 9 shows that the tangential velocity increases with α, especially near the interface. This suggests that higher permeability enhances lateral fluid motion within the shell, consistent with reduced internal resistance. Therefore, the tangential velocity profiles show less sensitivity to α but exhibit smoother gradients for higher permeability, indicating better momentum transfer across the interface. In Figure 10, microrotation increases with α, especially near the outer boundary of the shell. This reflects stronger rotational coupling due to enhanced fluid penetration and reduced confinement. Further, the microrotation field becomes more uniform with increasing α, indicating that the porous shell allows smoother rotational diffusion into the surrounding micropolar fluid.

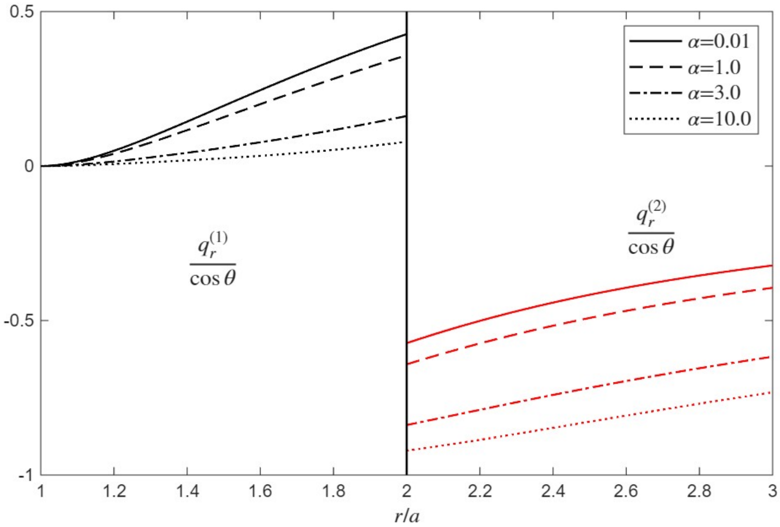

Figure 8. Normal velocity distribution for different permeability parameters at $\xi = 0.01, \kappa/\mu = 1.0$.

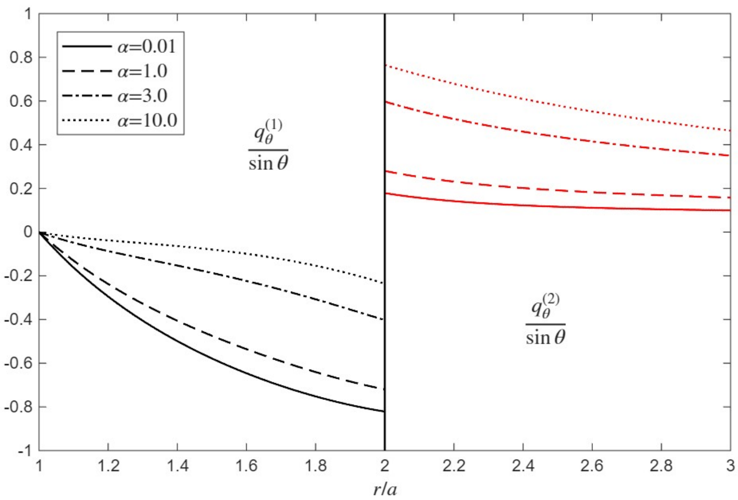

Figure 9. Tangential velocity distribution for different permeability parameters at $\xi = 0.01, \kappa/\mu = 1.0$.

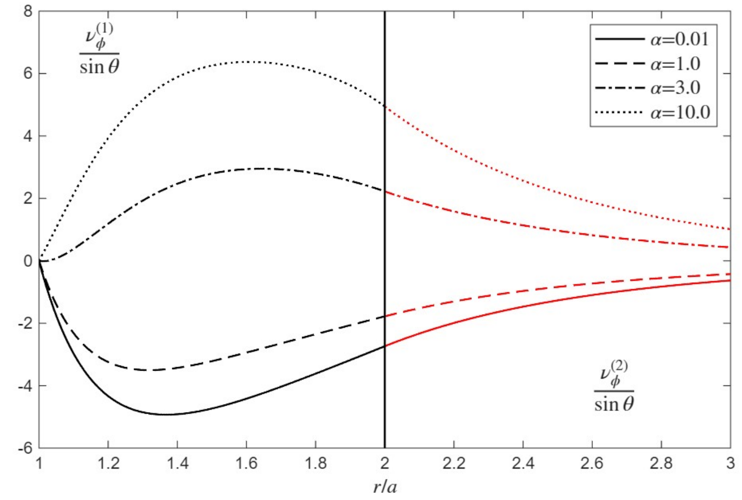

Figure 10. Microrotation distribution for different permeability parameters at $\xi = 0.01, \kappa/\mu = 1.0$.

Also, in Figure 11 explain the shear stress decreases with increasing α, showing that higher permeability reduces internal shear resistance. The peak stress shifts outward, consistent with fluid redistribution. The stress profiles become flatter and lower in magnitude as α increases, indicating reduced drag and smoother stress transmission into the external fluid. Figure 12 shows that the radial stress decreases with α, showing that higher permeability reduces pressure buildup within the shell. The stress gradient becomes less steep, reflecting improved fluid exchange. The radial stress field becomes more uniform with increasing α, indicating that the porous shell dampens stress discontinuities at the interface. Accordingly, Figure 13 exhibits the couple stress increases with α, especially near the interface, suggesting stronger microrotation gradients due to enhanced permeability. This reflects the increased rotational activity within the shell. The couple stress becomes more distributed and less concentrated, indicating that higher permeability allows rotational effects to diffuse more smoothly into the surrounding fluid. The permeability-dependent behavior of velocity, microrotation, and stress fields informs the design of soft capsules in biomedical transport, optimizing flow and drug release. In porous media engineering, it aids in predicting particle mobility and pressure gradients for enhanced oil recovery. These insights also support microfluidic device calibration for precise control of particle motion and stress distribution.

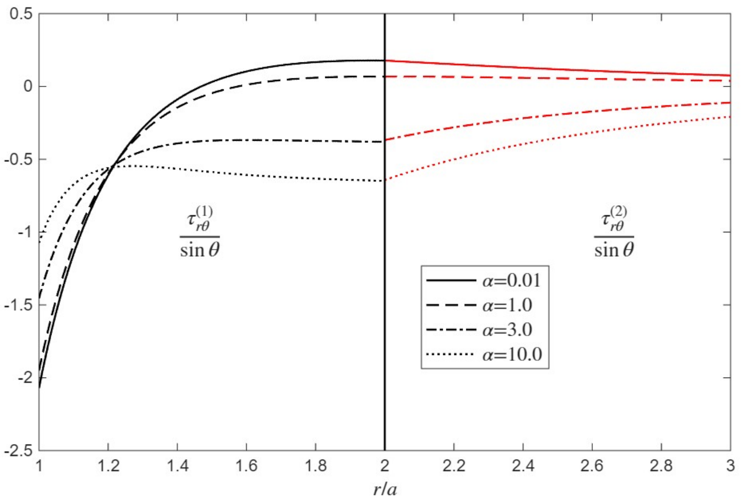

Figure 11. Tangential stress distribution for different permeability parameters at $\xi = 0.01, \kappa/\mu = 1.0$.

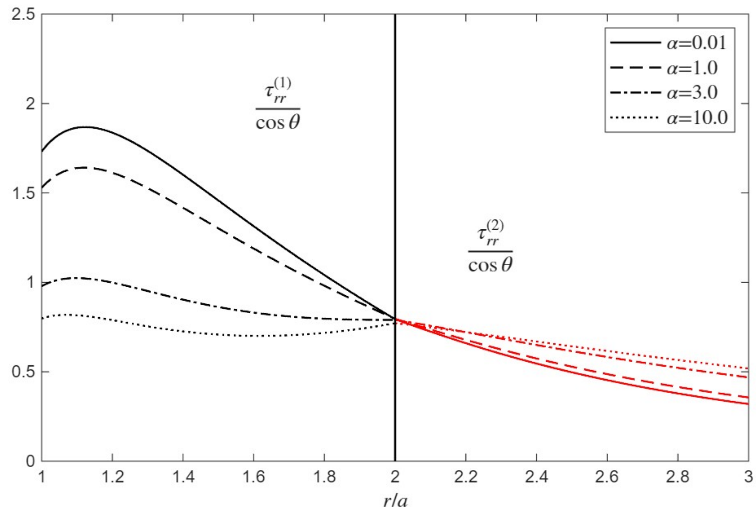

Figure 12. Normal stress distribution for different permeability parameters at $\xi = 0.01, \kappa/\mu = 0.5$.

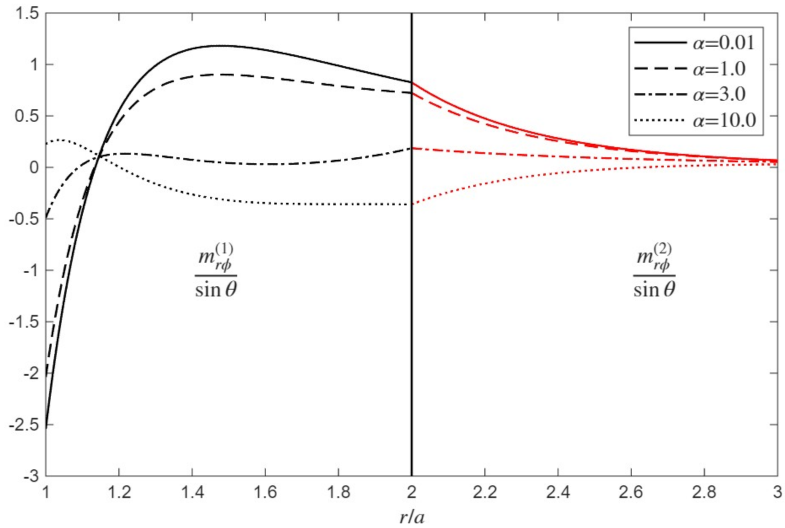

Figure 13. Tangential couple stress distribution for different permeability parameters at $\xi = 0.01$, $\kappa/\mu = 0.5$.

(3) Effects of the stress jump coefficient ξ:

In Figure 14, inside the porous shell (region 1), as ξ increases from 0.0 to 1.0, the magnitude of the inward radial velocity decreases, indicating stronger resistance at the interface; the velocity profile flattens, showing reduced fluid penetration into the shell. Outside the sphere (region 2), the radial velocity becomes more uniform with increasing ξ, reflecting smoother flow in the external micropolar fluid due to reduced interfacial momentum exchange. In Figure 15, the tangential velocity decreases with increasing ξ, especially near the interface, suggesting that higher stress jump suppresses lateral motion within the shell; the tangential velocity profiles show reduced peak values and smoother gradients as ξ increases, indicating dampened rotational flow across the boundary. In Figure 16, the microrotation decreases with increasing ξ, showing that stress jump inhibits rotational coupling at the interface; the peak shifts inward, and the profile becomes more confined; additionally, the microrotation field becomes flatter and lower in magnitude, indicating reduced rotational transmission into the surrounding fluid. In Figure 17, the shear stress decreases with increasing ξ, reflecting reduced tangential force transfer across the interface; the stress peak shifts inward and diminishes; the stress profile becomes smoother and less pronounced, indicating that higher stress jump dampens shear propagation into the external fluid. Moreover, in Figure 18, the radial stress decreases with increasing ξ, showing that interfacial resistance reduces pressure buildup within the shell; the gradient becomes less steep; in the outside region, the radial stress field becomes more uniform and lower in magnitude, indicating smoother stress transmission into the micropolar fluid. In Figure 19, the couple stress decreases with increasing ξ, especially near the interface, suggesting that stress jump suppresses microrotation gradients and internal torque; on the other side, the couple stress becomes more distributed and less concentrated, indicating reduced rotational influence from the porous shell into the surrounding fluid. Consequently, stress jump conditions are crucial in modeling interfacial resistance between porous coatings and surrounding fluids, enabling accurate predictions of drag and flow discontinuities. This is especially applicable in designing biomedical capsules, filtration membranes, and composite materials with layered microstructures.

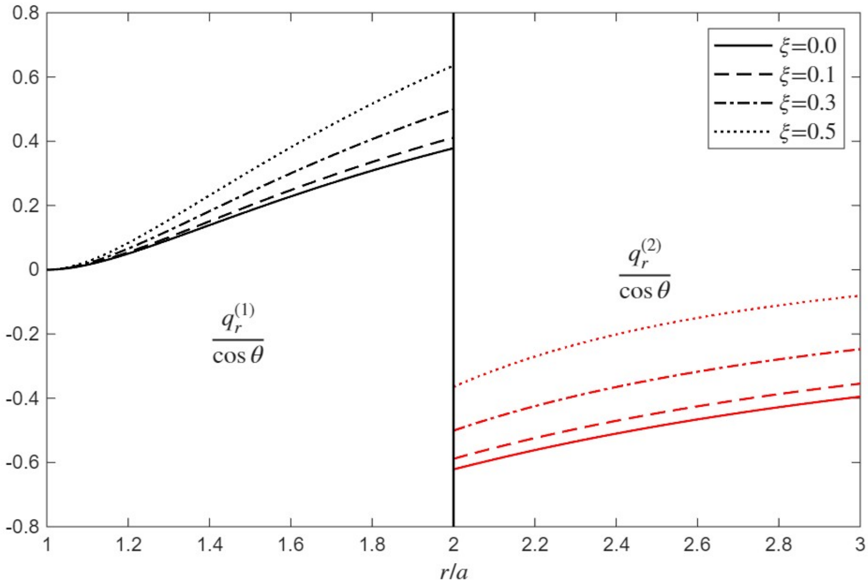

Figure 14. Normal velocity distribution for different stress jump parameters at $\alpha = 1.0, \kappa/\mu = 0.1$.

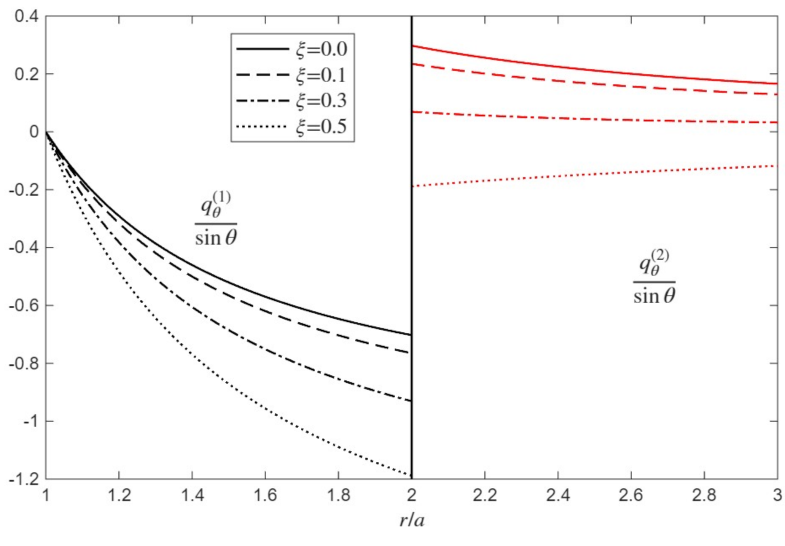

Figure 15. Tangential velocity distribution for different stress jump parameters at $\alpha = 1.0, \kappa/\mu = 0.1$.

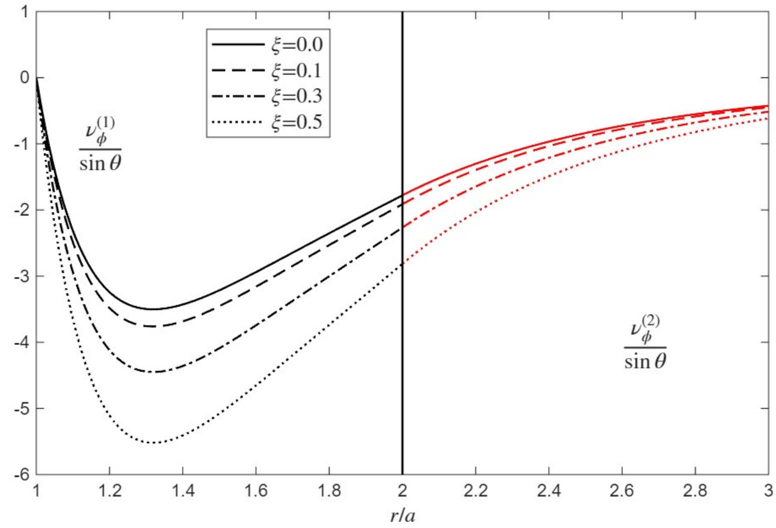

Figure 16. Microrotation distribution for different stress jump parameters at $\alpha = 1.0, \kappa/\mu = 0.1$.

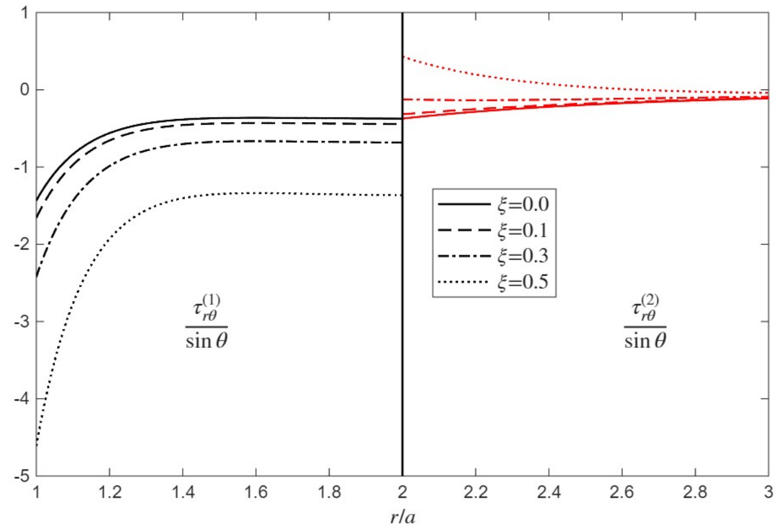

Figure 17. Tangential stress distribution for different stress jump parameters at $\alpha = 3.0, \kappa/\mu = 0.1$.

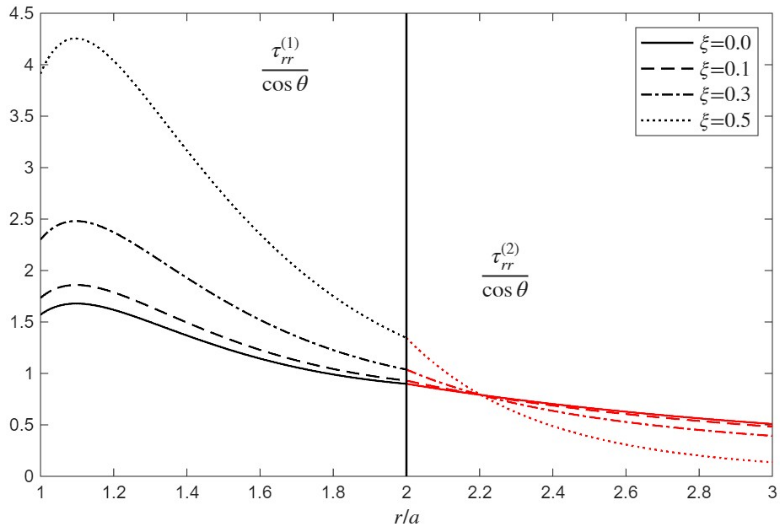

Figure 18. Normal stress distribution for different stress jump parameters at $\alpha = 3.0,\ \kappa/\mu = 0.1$.

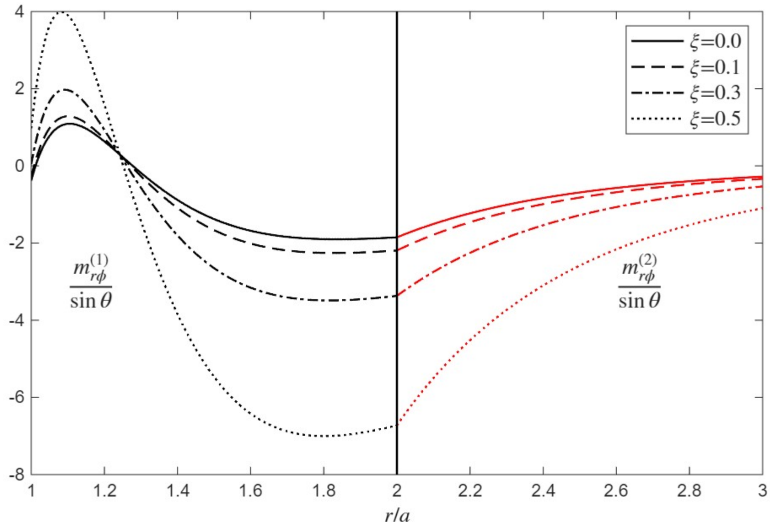

Figure 19. Tangential couple stress distribution for different stress jump parameters at $\alpha = 3.0$, $\kappa/\mu = 0.1$.

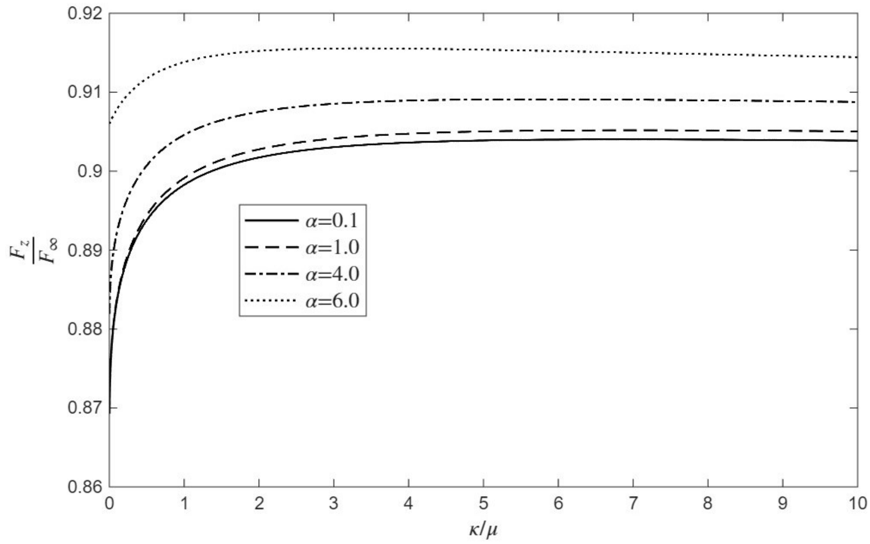

Figure 20. Normalized drag force for different permeability parameters at $\xi = 0.2$, $\epsilon = 0.3$, $\sigma = 1.1$.

(4) Parameter effects on the normalized drag force F_z/F_∞:

The normalized drag force F_z (plotted on the vertical axis in the figures) is analyzed as a function of the dimensionless micropolarity parameter κ/μ, where κ is the vortex viscosity and μ is the shear viscosity. The dependence of F_z is examined with respect to four key non-dimensional parameters: the permeability α, the stress jump coefficient ξ, the size ratio σ, and the parameter ϵ (the ratio of spin gradient viscosity to vortex viscosity coefficients).

1. *Effect of permeability α* Figure 20 illustrates the variation in normalized drag with κ/μ for different permeability values α. The normalized drag decreases monotonically as κ/μ increases for all α. A larger permeability ($\alpha = 6.0$) results in significantly lower drag across the entire range of κ/μ, while lower permeability ($\alpha = 0.1$) yields higher drag. The curves for different α diverge at low κ/μ and converge slightly at higher values. The permeability α represents the ease with which the fluid can pass through a porous medium or structured boundary. Higher permeability reduces flow resistance, thereby lowering the drag force. The convergence at high κ/μ indicates that the effect of permeability becomes less pronounced when micropolar effects (couple stresses) dominate.

2. *Effect of stress jump coefficient* ξ Figure 21 presents the normalized drag as a function of κ/μ for various stress jump coefficients ξ. Similar to the α case, drag decreases with increasing κ/μ, but the rate of decrease varies with ξ. A larger stress jump coefficient ($\xi = 0.8$) leads to *higher* drag, while a smaller coefficient ($\xi = 0.0$) results in lower drag. This is opposite to the effect of permeability. The stress jump coefficient ξ characterizes the discontinuity in shear stress at a fluid–solid interface due to micro-rotation effects. A larger ξ implies stronger resistance to the relative rotation between fluid particles and the boundary, increasing the drag. This parameter is critical in modeling microstructured or granular interfaces where classical no-slip conditions are inadequate.
3. *Effect of size ratio* σ Figure 22 shows the drag behavior on a log–log scale for different size ratios σ. The drag exhibits a sharp, power-law increase as κ/μ decreases toward very small values. At higher κ/μ, the drag saturates or increases slowly. Larger σ (e.g., $\sigma = 2.0$) produces a steeper rise in drag at low κ/μ, while smaller σ (e.g., $\sigma = 1.1$) gives a milder increase. The size ratio σ likely represents the ratio of a characteristic particle (or microstructure) size to a macroscopic length scale. A larger σ indicates stronger microstructural effects, leading to enhanced drag, especially in the regime where κ/μ is small (i.e., where classical viscous effects dominate over micropolar couple stresses). The divergence suggests a critical scaling behavior when the microstructure becomes comparable to the flow scale.
4. *Role of the micropolarity parameter* κ/μ Across all figures, κ/μ serves as the key independent variable controlling the transition between classical Newtonian and micropolar fluid behavior. For small κ/μ, the fluid behaves more like a Newtonian fluid, and drag is higher and more sensitive to α, ξ, and σ. For large κ/μ, micropolar effects (micro-rotations and couple stresses) become dominant, generally reducing the drag and diminishing the influence of permeability and stress jump.

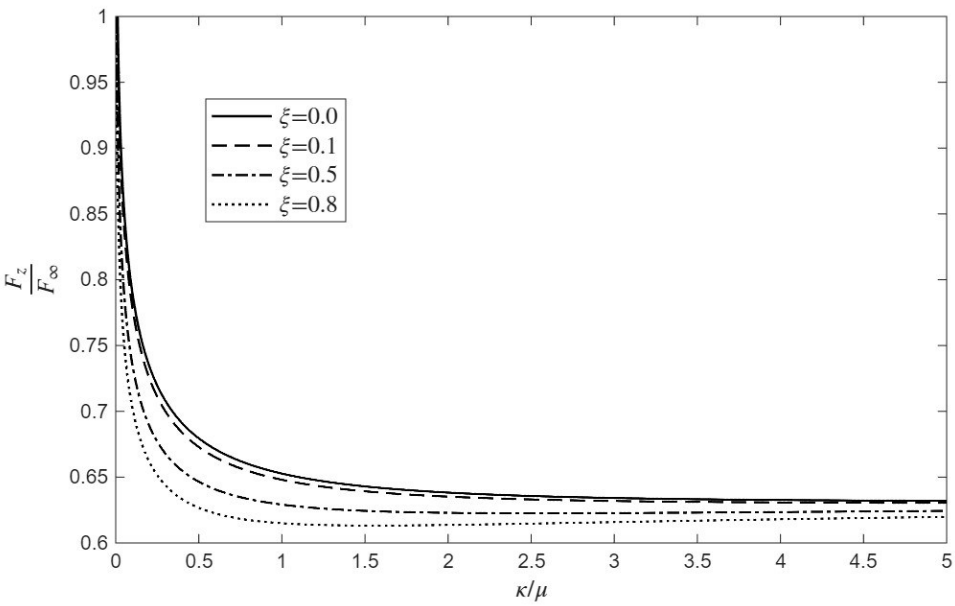

Figure 21. Normalized drag force for different stress jump parameters at $\epsilon = 0.3$, $\alpha = 3.0$, $\sigma = 2.0$.

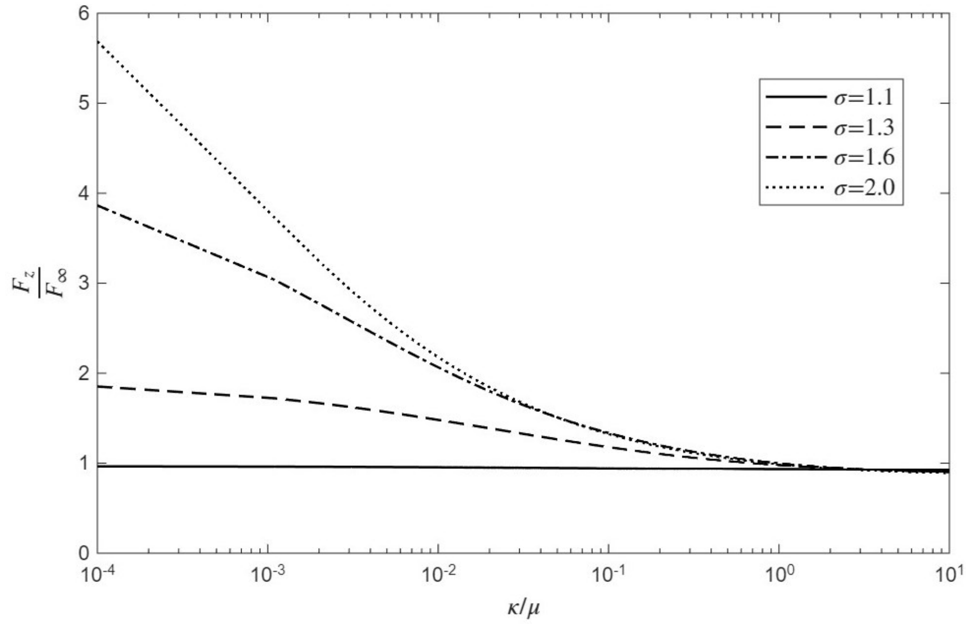

Figure 22. Normalized drag force for different size ratio at $\alpha = 10.0,\ \epsilon = 0.3,\ \xi = 0.5$.

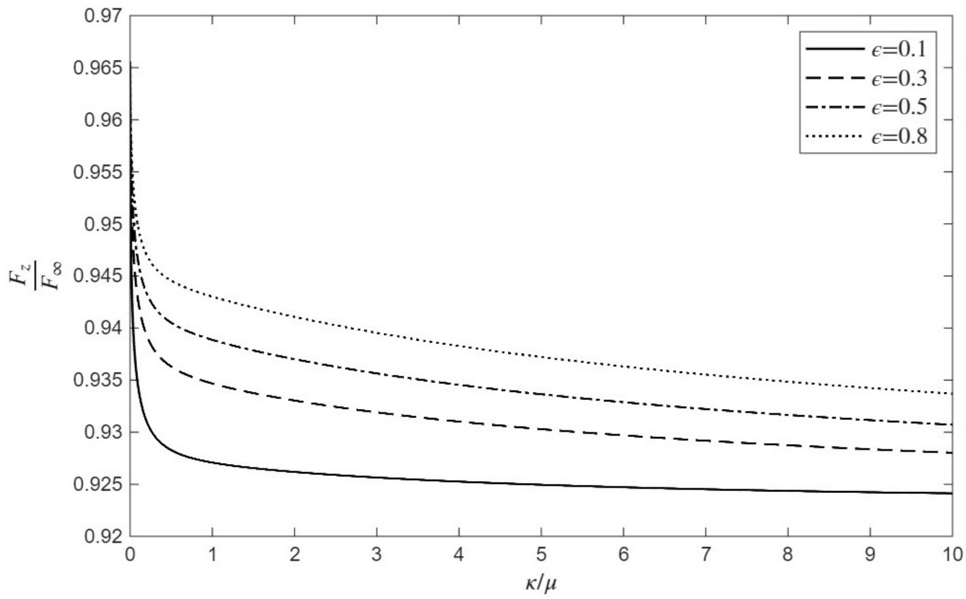

Figure 23. Normalized drag force for different ϵ at $\alpha = 10.0,\ \xi = 0.5,\ \sigma = 1.1$.

7. Conclusions

The detailed analysis of the velocity fields, microrotation, stresses, and couple stresses around a soft porous sphere immersed in a micropolar fluid reveals several important physical trends governed by the micropolarity, radial position, permeability, and interfacial stress jump conditions. Increasing the micropolarity parameter κ consistently suppresses both radial and tangential velocity components and reduces shear stresses, while simultaneously enhancing microrotation and couple stresses—highlighting the dual translational–rotational resistance characteristic of micropolar fluids. All flow and stress quantities exhibit strong radial dependence, with pronounced variations near the porous–fluid interface and gradual decay toward the core or the far field region; the porous shell significantly shapes the internal distributions, whereas the infinite micropolar medium smooths the external fields. The results show excellent agreement with established micropolar fluid theory, confirming that higher micropolarity reduces drag and modifies stress transmission in predictable ways, and validating the analytical–numerical framework used in this study. The main findings are:

1. The permeability parameter α plays a central role in regulating the interaction between the porous shell and the surrounding fluid. Increasing α reduces internal hydrodynamic resistance, enhances both translational and rotational motion within the shell, and smooths stress transitions across the interface. As permeability increases, the porous layer becomes more transparent to flow and microrotation, leading to reduced drag and diminished stress discontinuities. These findings confirm that permeability is a key tuning parameter for controlling hydrodynamic and microrotational behavior of soft particles in micropolar environments.
2. The stress jump parameter ξ introduces an additional layer of interfacial control. Higher values of ξ impose stronger resistance at the porous–fluid boundary, reducing both translational and rotational flow across the interface. As a result, velocity, microrotation, and stress fields become more confined, smoother, and lower in magnitude, demonstrating that β effectively regulates the degree of coupling between the porous shell and the external micropolar medium. Collectively, these trends underscore the importance of micropolarity, permeability, and interfacial stress conditions in shaping the hydrodynamic response of soft porous particles, offering valuable insights for applications involving complex fluids, microstructured materials, and particulate transport in micropolar environments.

Accordingly, negative values of the stress-jump parameter physically indicate that the tangential shear stress within the porous layer is greater than that in the adjacent free fluid at the interface. This situation may occur when the porous coating enhances momentum transfer due to high internal permeability, anisotropic microstructure, or surface treatments that promote stronger fluid–matrix interaction. Experimentally, such conditions can be achieved through engineered porous coatings, microstructured interfaces, or controlled surface modifications that alter interfacial transport properties. Therefore, negative stress-jump values represent physically realizable interfacial configurations rather than purely mathematical assumptions.

This study provides theoretical insight into the effects of permeability (α), stress jump coefficient (ξ), size ratio (σ), and micropolarity (κ/μ) on normalized drag in a micropolar fluid. However, several limitations exist: the parameters are treated phenomenologically without explicit constitutive models; the analysis is restricted to steady, linear flows; the role of ϵ remains unexplored; and the predictions lack experimental validation. Despite these limitations, the findings have practical implications. In porous media flows, increasing α reduces drag, especially at low κ/μ. In microfluidic devices, minimizing ξ lowers drag when handling suspensions. In colloidal systems, controlling σ avoids excessive drag at low κ/μ. Future work should include: developing explicit physical models for α, ξ, σ, and ϵ; experimental validation with model micropolar fluids; extension to unsteady, inertial, and nonlinear regimes; investigation of complex geometries; exploration of multiphase and non-Newtonian extensions; incorporation of coupled physics; optimization for drag control; and application to biological and industrial flows.

The present analysis provides several directions for future research. First, the theoretical framework developed here can be extended to incorporate elastic deformation of the porous layer, non-linear micropolar effects, or time-dependent flow conditions to better represent realistic biological and engineering systems. Second, experimental validation of the predicted hydrodynamic resistance and stress-jump behavior would significantly enhance the practical relevance of the model. Finally, the interaction of multiple soft particles and the influence of confined geometries or external fields (e.g., magnetic or electric) offer promising avenues for further investigation. Such extensions would contribute to a deeper understanding of transport phenomena involving coated or gel-like particles in complex fluids.

Funding: The author extends the appreciation to the Deanship of Scientific Research and Libraries in Princess Nourah bint Abdulrahman University for funding this research work through the Supporting Publication in Top-Impact Journals Initiative (SPTIF-2026).

Data Availability Statement: The original contributions presented in this study are included in the article. Further inquiries can be directed to the corresponding author.

Acknowledgments: The author extends the appreciation to the Deanship of Scientific Research and Libraries in Princess Nourah bint Abdulrahman University for funding this research work through the Supporting Publication in Top-Impact Journals Initiative (SPTIF-2026).

Conflicts of Interest: The author declares no conflicts of interest.

References

1. Johnson, K.L. *Contact Mechanics*; Cambridge University Press: Cambridge, UK, 1985.
2. Cundall, P.A.; Strack, O.D.L. A discrete numerical model for granular assemblies. *Géotechnique* **1979**, *29*, 47–65. [CrossRef]
3. Zhu, H.P.; Zhou, Z.Y.; Yang, R.Y.; Yu, A.B. Discrete particle simulation of particulate systems: A review. *Chem. Eng. Sci.* **2007**, *62*, 3378–3396. [CrossRef]
4. Bear, J. *Dynamics of Fluids in Porous Media*; Dover: New York, NY, USA, 1972.
5. Alizadeh, A.; Sahimi, M. Flow of deformable particles in porous media. *Phys. Rev. E* **2014**, *90*, 043013.
6. Decuzzi, P.; Ferrari, M. The adhesive strength of non-spherical particles mediated by specific interactions. *Biomaterials* **2006**, *27*, 5307–5314. [CrossRef] [PubMed]
7. Eringen, A.C. Theory of micropolar fluids. *J. Math. Mech.* **1966**, *16*, 1–18. [CrossRef]
8. Lukaszewicz, G. *Micropolar Fluids: Theory and Applications*; Birkhäuser: Basel, Switzerland, 1999.
9. Ariman, T.; Turk, M.A.; Sylvester, N.D. Microcontinuum fluid mechanics—A review. *Int. J. Eng. Sci.* **1973**, *11*, 905–930. [CrossRef]
10. El Sapa, S. Cell models for micropolar fluid past a porous micropolar fluid sphere with stress jump condition. *Phys. Fluids* **2022**, *34*, 082014. [CrossRef]
11. Jhuang, L.J.; Keh, H.J. Slow axisymmetric rotation of a soft sphere in a circular cylinder. *Eur. J. Mech. B Fluids* **2022**, *95*, 205–211. [CrossRef]
12. Chen, Y.C.; Keh, H.J. Slow translation of a composite sphere in an eccentric spherical cavity. *Fluids* **2024**, *9*, 154. [CrossRef]
13. Ragab, K.E.; Faltas, M.S. The creeping movement of a soft colloidal particle normal to a planar interface. *Phys. Fluids* **2024**, *36*, 072106. [CrossRef]
14. Chou, Y.F.; Keh, H.J. Axisymmetric slow rotation of coaxial soft/porous spheres. *Molecules* **2024**, *29*, 3573. [CrossRef] [PubMed]
15. Brinkman, H.C. A calculation of the viscous force exerted by a flowing fluid on a dense swarm of particles. *Appl. Sci. Res.* **1947**, *1*, 27–34. [CrossRef]
16. Faltas, M.S.; Sherief, H.H.; Allam, A.A.; Ahmed, B.A. Axisymmetric motion of a slip spherical particle in the presence of a Brinkman interface with stress jump. *Eur. J. Mech. B Fluids* **2021**, *90*, 73–84. [CrossRef]
17. Hamdan, M.H.; Kamel, M.T. Polar fluid flow through variable-porosity, isotropic porous media. *Spec. Top. Rev. Porous Media Int. J.* **2011**, *2*, 145–155. [CrossRef]
18. Khanukaeva, D.Y.; Filippov, A.N. Isothermal flows of micropolar liquids: Formulation of problems and analytical solutions. *Colloid J.* **2018**, *80*, 14–21. [CrossRef]
19. El Sapa, S. Interaction between a non-concentric rigid sphere immersed in a micropolar fluid and a spherical envelope with slip regime. *J. Mol. Liq.* **2022**, *351*, 118611. [CrossRef]
20. Ramkissoon, H.; Majumdar, S.R. Drag on an axially symmetric body in the Stokes' flow of a micropolar fluid. *Phys. Fluids* **1976**, *19*, 16–20. [CrossRef]